

Adaptive Mesh Refinement for Topology Optimization with Discrete Geometric Components

Shanglong Zhang¹, Arun L. Gain², and Julián A. Norato^{*1}

¹Department of Mechanical Engineering, University of Connecticut

²VPDS Inc.

Abstract

This work introduces an Adaptive Mesh Refinement (AMR) strategy for the topology optimization of structures made of discrete geometric components using the geometry projection method. Practical structures made of geometric shapes such as bars and plates typically exhibit low volume fractions with respect to the volume of the design region they occupy. To maintain an accurate analysis and to ensure well-defined sensitivities in the geometry projection, it is required that the element size is smaller than the smallest dimension of each component. For low-volume-fraction structures, this leads to finite element meshes with very large numbers of elements. To improve the efficiency of the analysis and optimization, we propose a strategy to adaptively refine the mesh and reduce the number of elements by having a finer mesh on the geometric components, and a coarser mesh away from them. The refinement indicator stems very naturally from the geometry projection and is thus straightforward to implement. We demonstrate the effectiveness of the proposed AMR method by performing topology optimization for the design of minimum-compliance and stress-constrained structures made of bars and plates.

1 Introduction

Topology optimization is a powerful tool to explore structural designs given performance and resource requirements. By relating the design parameterization with a fixed discretization for analysis, efficient optimization algorithms can be used to determine the optimal material distribution. The prevalent classes of methods for topology optimization are the density-based method and the level-set method (cf., [1]). In the former, the design region is discretized into a voxel-like grid using the finite element mesh, with a continuous pseudodensity variable assigned to each element that indicates the presence or absence of material at that element. In level-set methods, the boundary of the design is represented by the zero level set of a function, and the optimal design is obtained by evolving the zero level set. Both classes of techniques render organic designs, which then need to be translated into a Computer-Aided Design (CAD) model adding considerations for manufacturability. Design modifications are inevitably introduced in this translation, hence the final design departs from its optimum. This departure is more pronounced when the structure is fabricated using stock material by joining components of fixed shape but variable dimensions.

To address this difficulty, several works have recently been proposed in topology optimization to produce designs made exclusively of discrete geometric components. Since these geometric components have high-level geometry representations, these techniques ease the transition to a CAD model that more closely resembles the optimal topology. One category of these techniques is the geometry projection method [2, 3, 4, 5, 6, 7, 8, 9, 10]. This technique smoothly maps the high-level description of the geometric components onto a fixed density grid at each optimization iteration to circumvent re-meshing upon design changes. This method has been successfully applied to the design of structures made of straight bars [3], flat plates [4, 6] curved plates [8] and geometric primitives represented by the super-formula [10]. It has been applied both to compliance minimization problems as well as problems with stress considerations [7]. To further improve the manufacturability of the optimal design, some geometric constraints have been introduced, such as bounds on the dimensions of the components [3, 4], ensuring a minimum separation between geometric components to allow for tool access [6], and ensuring geometric components are fully contained within irregular, non-convex design regions to avoid impractical cuts [8]. The

*Corresponding author: julian.norato@uconn.edu

geometry projection method has also been used for the topology optimization of multimaterial lattices [11] and structures [9].

The other major category of topology optimization techniques with geometric components is the Moving Morphable Components (MMC) method [12, 5, 13, 14, 15, 16, 17, 18, 19], along with its related technique of Moving Morphable Voids (MMV) [16, 20, 21]. In these techniques, the geometric solid components or voids are represented via a topological description function, which corresponds to a level set description of the boundaries. This function is then mapped onto the analysis domain via a smooth Heaviside function.

Topology optimization techniques typically employ a fixed finite element mesh with uniform (or close-to-uniform) element size. The element size should not be too large, otherwise the design and the structural response cannot be accurately captured. In the case of thin structural components, it is desirable to have multiple elements across the component thickness. In the context of geometry projection methods, a further requirement is imposed on the element size that requires the maximum element size must be less than half of the thickness of the component to ensure well-defined, continuous sensitivities [3, 4]. These requirements dictate the maximum element size that can be used in geometry projection methods to obtain good results. Structures made of stock material often occupy a relatively small fraction of the volume of the design region; and the thickness of the components is very small in relation to the dimensions of the design region. If a uniform element size mesh is used, the foregoing mesh size requirements together with the volume fractions and dimension ratios encountered in practice for structures made of stock material lead to very large meshes with tens of millions of elements. Therefore, a natural idea is to employ a coarse mesh for regions where there is pure solid or void, and a fine mesh near the boundaries of the geometric components. In this work, we propose an Adaptive Mesh Refinement (AMR) strategy for the geometry projection method to reduce the total number of elements in the mesh while keeping the same accuracy for the geometry projection and the analysis.

Several AMR approaches have been proposed in the literature to improve the computational efficiency and solution accuracy in density-based topology optimization. Most methods use some function of the density field and/or an analysis error estimator as a refinement indicator. The earliest of these methods is presented in [22], which presents a strategy commonly used in subsequent methods. In this strategy, a complete optimization is performed on a coarse, uniform size mesh, whose resulting density field is used to refine the mesh and perform a subsequent optimization. Some works (e.g., [23]) also use the mesh quality and an analysis error estimator computed on the previous mesh as additional criteria for refinement. Other density-based AMR techniques that follow the optimize \rightarrow refine strategy based on one or more of the aforementioned refinement criteria include [24, 25, 26, 27, 28]. All of these methods aim to have a coarser mesh in the void region; some use a finer mesh for regions that are solid or near the boundary, while others only refine a band of elements around the boundary, which leads to additional computational savings.

A different AMR strategy consists of adaptively refining the mesh upon each design change in the optimization. Such a technique is proposed in [29], where it is shown that this strategy leads to better designs, since in the foregoing strategy the early optimization runs on coarse meshes can lock into poor local minima. Another contribution of this work is that an additional layer of elements near the material boundary is marked for refinement to improve the optimality of the final design. This approach allows de-refinement to coarsen the fine mesh in void regions as the material boundary propagates in the optimization. Other techniques that employ the design step \rightarrow refine strategy include [30, 31, 32, 33, 34]. It is worth noting that the works in [31, 34] consider stress-based topology optimization and thus have an additional motivation for doing AMR, which is to improve the accuracy of the stresses.

All of the aforementioned AMR schemes are for density-based topology optimization methods. In [21], AMR is performed at the boundary of holes described via B-splines in the MMV method to improve the accuracy of stress calculation. Elements that are cut by the material boundary, which is given by the boundary of the B-spline, are marked for further refinement. The analysis is solved using the extended finite element method (XFEM).

In this work, we propose an AMR strategy for topology optimization with discrete geometric components using the geometry projection method. To this end, we combine and adapt several of the aforementioned AMR strategies employed in density-based techniques. In our method, the mesh is refined and coarsened upon each design change in the optimization based solely on the geometric description of the components. The geometry projection method provides a natural way to define the refinement indicator. We only refine elements on a band around the material boundary, leading to a finer mesh near the material boundary and a coarser mesh at the pure solid or void regions. We note that we do not employ any error estimator from the analysis as refinement indicator, since our primary goal is to reduce the total number of elements for large problems. The remainder of the paper is organized as follows. Section 2 briefly describes the geometry projection method. Section 3 presents the AMR strategy. The optimization and computer implementation are detailed in Section 4. We provide numerical examples in Section 5 to demonstrate the effectiveness of the proposed method. Finally, we draw conclusions in Section 6.

2 Geometry projection

For the topology optimization with geometric components, we map the geometric components onto a fixed analysis mesh to circumvent re-meshing upon design changes. To this end, we employ the geometry projection method [35, 3] to establish a differentiable map between the parametric description of the geometry and a density field defined over a fixed finite element grid. With the projected density, we can perform the finite element primal and sensitivity analyses in a manner similar to the density-based method. Since the geometry projection is smooth, a continuous design sensitivity of the geometric components can be readily computed via the chain rule.

In what follows, we briefly describe the geometry projection technique, starting with the geometry projection of a single geometric component. We first consider a ball-shaped sampling window $B_{\mathbf{x}}^R$ of radius R centered at \mathbf{x} . The projected density at \mathbf{x} is computed as the area fraction of the circular segment (or volume fraction of spherical cap in 3-d) of height $R - d$ (see Fig. ??):

$$\rho_i(\mathbf{x}) := \frac{|B_{\mathbf{x}}^R \cap \omega_i|}{|B_{\mathbf{x}}^R|} \quad (1)$$

where ω_i denotes the region of space occupied by component i , and $|\cdot|$ is the area (or volume). Assuming that the portion of $\partial\omega_i$ that intersects the ball, $\partial\omega_i \cap B_{\mathbf{x}}^R$, can be approximated as a straight line in 2-d, the projected density of Eq. 1 can be computed as a function of the signed distance $d(\mathbf{x})$ from \mathbf{x} to the boundary of the component $\partial\omega_i$ as:

$$\rho_i(d(\mathbf{x}), R) := \begin{cases} 0 & \text{if } d > R \\ \frac{1}{\pi R^2} \left[R^2 \arccos\left(\frac{d}{R}\right) - d\sqrt{R^2 - d^2} \right] & \text{if } -R \leq d \leq R \\ 1 & \text{if } d < -R \end{cases}$$

Conversely, if for 3-dimensional problems we assume that $\partial\omega_i \cap B_{\mathbf{x}}^R$ can be approximated as a flat surface, the projected density can be computed as:

$$\rho_i(d(\mathbf{x}), R) := \begin{cases} 0 & \text{if } d > R \\ \frac{1}{2} + \frac{d^3}{4R^3} - \frac{3d}{4R} & \text{if } -R \leq d \leq R \\ 1 & \text{if } d < -R \end{cases}$$

The argument \mathbf{x} is removed from the signed distance on the right-hand side of the above expressions for conciseness. The signed distance is a function the vector of design variables \mathbf{z}_i that parameterize component i , i.e., $d(\mathbf{x}, \mathbf{z}_i)$. Different expressions of d can be derived for different component shapes. For instance, the signed distance function of bars, flat plates, and curved plates modeled with offset surfaces are given in [3], [4], and [8]; for the sake of brevity, and since we use several of these component geometries in this work, we refer the reader to the afore cited works for these expressions. The projected density is computed every time the design changes.

Fig. 2 shows the projected density of a bar (modeled as an offset surface of a straight line segment, cf., [3]—i.e., the line segment is the medial axis of the bar). The idea behind the AMR scheme we propose in this work is simple: the projected density can be used as a refinement indicator. For instance, elements that are fully solid or fully void ($\rho = 1$ or $\rho = 0$, respectively) can be meshed with a coarse mesh, while elements with an intermediate density ($0 < \rho < 1$) can be meshed with a fine mesh. We do not directly use the projected density as a refinement indicator for reasons that we elaborate on later—however, this is the essential idea.

As in ersatz material methods, the density is used to modified the material properties to reflect a fully or partially solid material, or void. In addition to the projected density of Eq. 1, we ascribe a size variable $\alpha_i \in [0, 1]$ to each geometric component, which is penalized in the spirit of Solid Isotropic Material Penalization (SIMP). This is a unique and key feature of the geometry projection method that allows the optimizer to entirely remove a geometric component i from the design. Using the projected density ρ_i and the size variable α_i , we now define an *effective density* as:

$$\hat{\rho}_i(\mathbf{x}, \mathbf{z}_i, s, R) := \alpha_i^s \rho_i(\mathbf{x}, \mathbf{z}_i, R) \quad (2)$$

where s is the SIMP penalization power. Thanks to the size variable, a component i may have a projected density of unity at a point \mathbf{x} , but if its size variable α_i equals zero, the effective density of that component at \mathbf{x} is also zero.

We note that the effective density constitutes an implicit geometric representation of the component. Therefore, when multiple components overlap, we perform their Boolean union, which for implicit representations corresponds to the maximum function, i.e.:

$$\tilde{\rho}(\mathbf{x}, \mathbf{z}, s, R) := \max_i \hat{\rho}_i(\mathbf{x}, \mathbf{z}_i, s, R), \quad i = 1, \dots, n \quad (3)$$

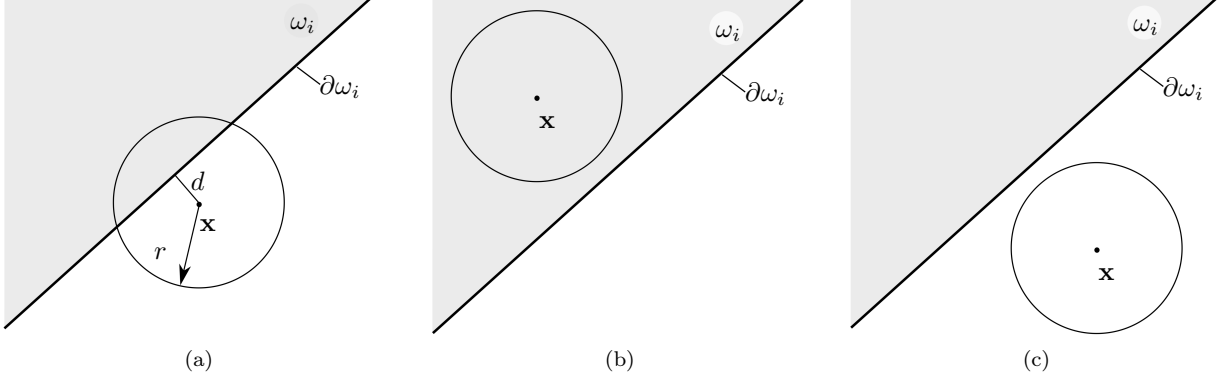


Figure 1: Geometry projection for various points \mathbf{x} with respect to a geometric component i : (a) partially intersecting ω_i , with $0 < \rho_i < 1$; (b) inside of ω_i , with $\rho_i = 1$; and (c) outside of ω_i , with $\rho_i = 0$.

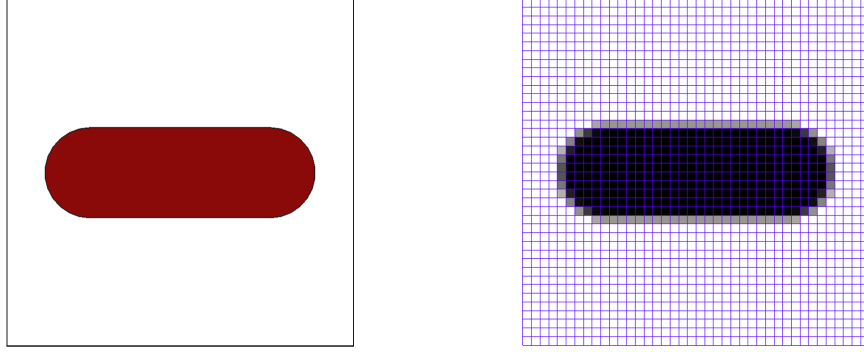


Figure 2: Geometry projection of a solid bar onto a uniform finite element grid

In this expression, $\tilde{\rho}(\mathbf{x}, \mathbf{z}, s, R)$ is a *composite density* from all n components, and $\mathbf{z} := [\mathbf{z}_1^T, \dots, \mathbf{z}_n^T]^T$ denotes the vector of design variables, noting that \mathbf{z}_i now includes α_i . Since the maximum function is not differentiable, we replace it with a smooth approximation so that we can use efficient gradient-based optimizers. Here, we use a lower-bound Kreisselmeier–Steinhauser (KS) function, which has the form

$$\max_i x_i \approx KS_{\max}(\mathbf{x}) := \frac{1}{k} \ln \left(\frac{1}{n} \sum_{i=1}^n e^{kx_i} \right) \quad (4)$$

with aggregation coefficient k . We apply this approximation to the composite density $\tilde{\rho}$ in Eq. 3 to obtain

$$\tilde{\rho}_{ks}(\mathbf{x}, \mathbf{z}, s, R) \approx \tilde{\rho}_{KS}(\mathbf{x}, \mathbf{z}, s, R, k) := KS_{\max}(\hat{\rho}(\mathbf{x}, \mathbf{z}, s, R)) \quad (5)$$

where $\hat{\rho}$ is the vector of effective densities. With this smooth composite density, we now define the elasticity tensor of the ersatz material as:

$$\mathbb{C}(\mathbf{x}, \mathbf{z}, s, R) := [\rho_{\min} + \tilde{\rho}_{ks}(\mathbf{x}, \mathbf{z}, s, R)(1 - \rho_{\min})] \mathbb{C}_o \quad (6)$$

The small lower bound $0 < \rho_{\min} \ll 1$ prevents an ill-posed analysis. In the finite element analysis, we use a uniform composite density for each element, with the projected density computed at its centroid.

3 Adaptive mesh refinement

For a convenient demonstration of the mesh refinement strategy we describe in the sequel, we discretize the design region using bilinear quadrilateral elements for 2-dimensional problems and trilinear hexahedral elements for 3-dimensional problems. The mesh refinement is performed by successively subdividing quadrilaterals in four

using a quadtree strategy, and octahedrons in eight using an octree strategy. In Figs. 3a and 3b, the element on the top right corner is refined by subdividing the parent element into smaller children elements. When neighboring elements have different levels of refinement, there will be ‘hanging nodes’ along element edges (indicated with circles in Fig. 3). These hanging nodes introduce incompatibility to the finite element solution across element edges, therefore constraint equations on the degrees of freedom must be imposed to ensure continuity. As usual in these refinement schemes, neighboring elements are required to differ by no more than one level of refinement for ease of implementation. Figs 3c and 3d show examples of mesh refinements that violate this single-level mesh-incompatibility requirement. To satisfy this requirement, if two neighboring elements already differ by a level of refinement and the element with the finer mesh is marked for refinement, then the other element will be marked for refinement too. In the case of Figs 3c and 3d, refinement is required for the left-top and left-top-front elements respectively.

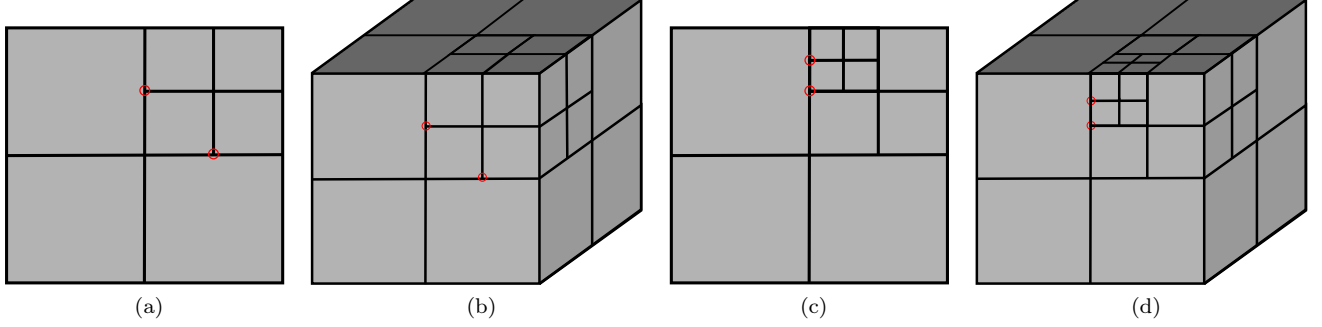


Figure 3: Mesh refinement by subdivision of (a and c) quadrilateral and (b and d) hexahedral elements. The refinements in (a) and (b) satisfy the single-level mesh-incompatibility requirement, while the refinements in (c) and (d) violate it.

To mark an element for refinement we require a refinement criterion. In the case of topology optimization with discrete geometric components, we seek a refinement indicator that accounts not only for the geometric parameters of the component, but also for its size variable. We first discuss for simplicity the case of a single component. In this case, if the component has a size variable of unity, we would like the underlying mesh to be coarse both inside and outside of the component and fine near its boundaries; and if the size variable is zero, we would like the underlying mesh to be coarse in the region occupied by the component. Therefore, a suitable refinement indicator for a single component is the effective density of Eq. 2. That is, an element e is marked for refinement if its effective density satisfies

$$0 < \hat{\rho}^e \leq \rho_{th} \lesssim 1 \quad (7)$$

where ρ_{th} is a threshold effective density above which the element is considered to be close to solid.

Based on this refinement indicator, the proposed AMR process for a single component is as follows. 1) We start with a mesh whose elements all have a size corresponding to the coarsest level, and we compute the effective density for all the elements; 2) elements are marked for refinement if they satisfy Eq. 7; and 3) marked elements are refined once by subdivision. If additional levels of refinement are desired, then the process is repeated, i.e., the effective density is computed for all elements in the refined mesh of step 2, and elements are subsequently marked for refinement based on the aforementioned criterion, but also if they violate the single-level mesh-incompatibility requirement.

The AMR process for a structure made of a single solid bar (i.e., $\alpha = 1$) is now illustrated for two levels of refinement. The first level of refinement is shown in the top row of Fig. 4. First, the composite density is computed on a coarse grid (Fig. 4a). We use a sampling window radius R corresponding to the circle that circumscribes the element to compute its effective density $\hat{\rho}^e$ (in this 2-dimensional example, if the element e size is h^e , then $R = \sqrt{2}h^e/2$). We then mark elements for refinement based on the refinement criterion of Eq. 7, shown in Fig. 4b. Next, we refine the marked elements by subdivision to produce the mesh shown in Fig. 4c. We repeat the geometry projection on this refined mesh and re-compute the element effective densities (Fig. 4d). With these new densities, we perform an additional level of refinement, as shown in the bottom row of Fig. 4. In this level, we not only mark elements for refinement based on the refinement indicator, but also if they violate the single-level mesh-incompatibility requirement. Additional levels of refinement follow the same procedure. We note that, since the mesh refinement is based on the projected density, the refined mesh provides a better resolution of the geometry

of the component, and the resolution of course increases with additional levels of refinement, as can be seen by comparing Figs. 4d and 4h.

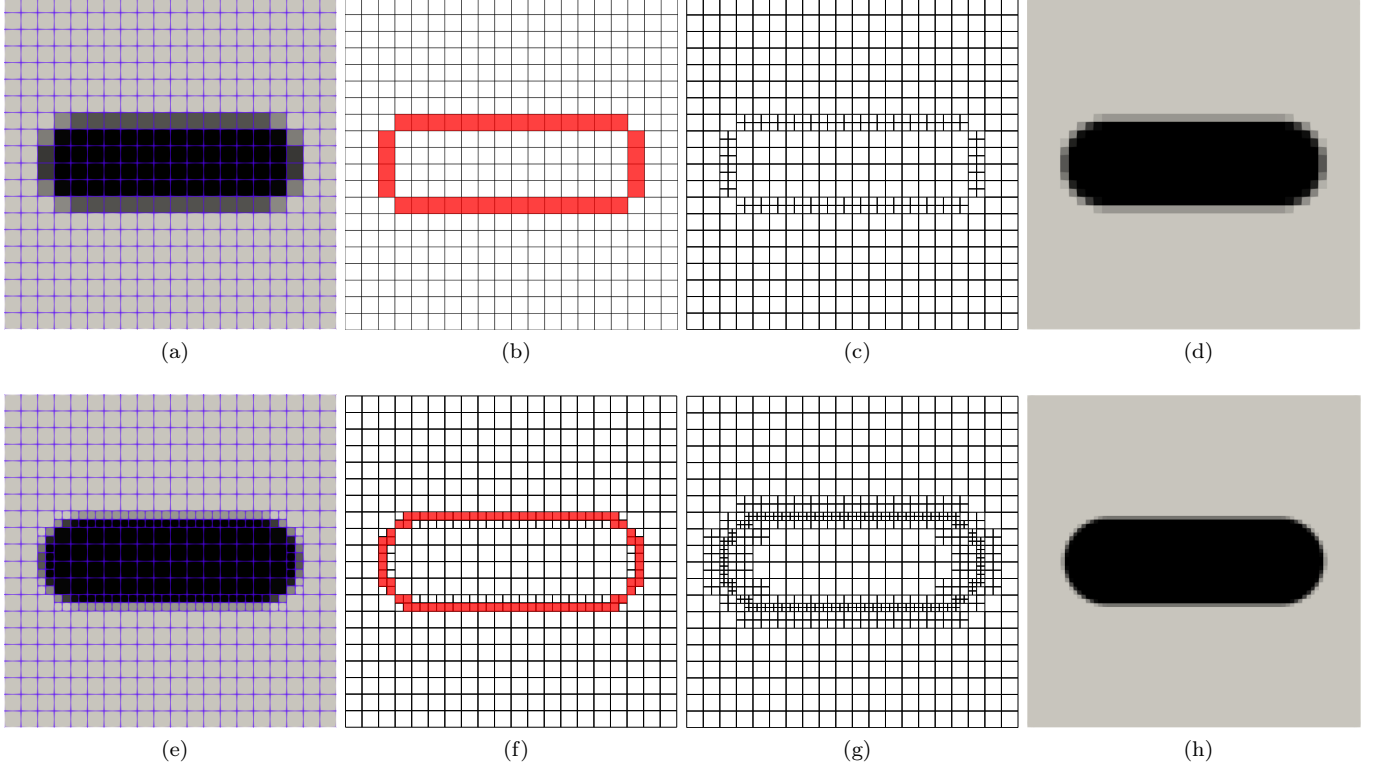


Figure 4: Mesh refinement of a single component based on its effective density. Top: first level of refinement; bottom: second level of refinement. (a and e) effective density before refinement; (b and f) elements marked for refinement; (c and g) refined mesh; and (d and h) effective density after refinement.

Since $\hat{\rho}^e$ is a function of the size variable of the component, different values of the size variable α will result in different refined meshes. Fig. 5 demonstrates the effect of values of the size variable on the mesh refinement. When $\alpha = 1$, only elements near the boundary of the bar are refined (Fig. 5a). When α has an intermediate value (such that $\hat{\rho}^e < \rho_{th}$), the entire region occupied by the bar is refined, which guarantees elements with intermediate effective densities are always refined. Finally, if $\alpha = 0$, the bar is effectively removed from the design, hence no mesh refinement is performed, as shown in Fig. 5d.

The aforementioned refinement strategy may lead to an inconsistent level of refinement (i.e., elements of different sizes) along the boundary of the component. Fig. 6a exemplifies this situation, where we observe that the element size is not consistent along the boundary of the bar due to the orientation of the bar. As demonstrated in [29] for density-based topology optimization, this inconsistency may lead to suboptimal designs. A solution to this issue, proposed in [29], is to increase the size of the band of elements around the boundary that are marked for refinement. It is straightforward to adapt this strategy in our method by increasing the radius R of the sampling window used to compute the effective density. For example, Fig. 6b shows the refined mesh when we use a radius that equals twice the radius of the circumscribing circle, i.e., $R = \sqrt{2}h^e$. In effect, doubling R is roughly equivalent to adding an additional layer of elements to the band, as shown in Fig. 7. We therefore use this increased sample window radius for the mesh refinement in all of our examples. We note, however, that when we compute the effective density to obtain the ersatz material of Eq. 6, the circumscribing sampling window radius is still used to obtain a more accurate geometry projection (note that, for a single bar, the composite density equals the effective density of the bar).

The above discussion considered only a single component. When considering multiple components, we simply impose the same refinement criterion of Eq. 7 on the composite density of Eq. 5, i.e.:

$$0 < \hat{\rho}_{ks}^e \leq \rho_{th} \lesssim 1 \quad (8)$$

When considering multiple bars, one important consideration is that the lower-bound KS-function Eq. 4 underes-

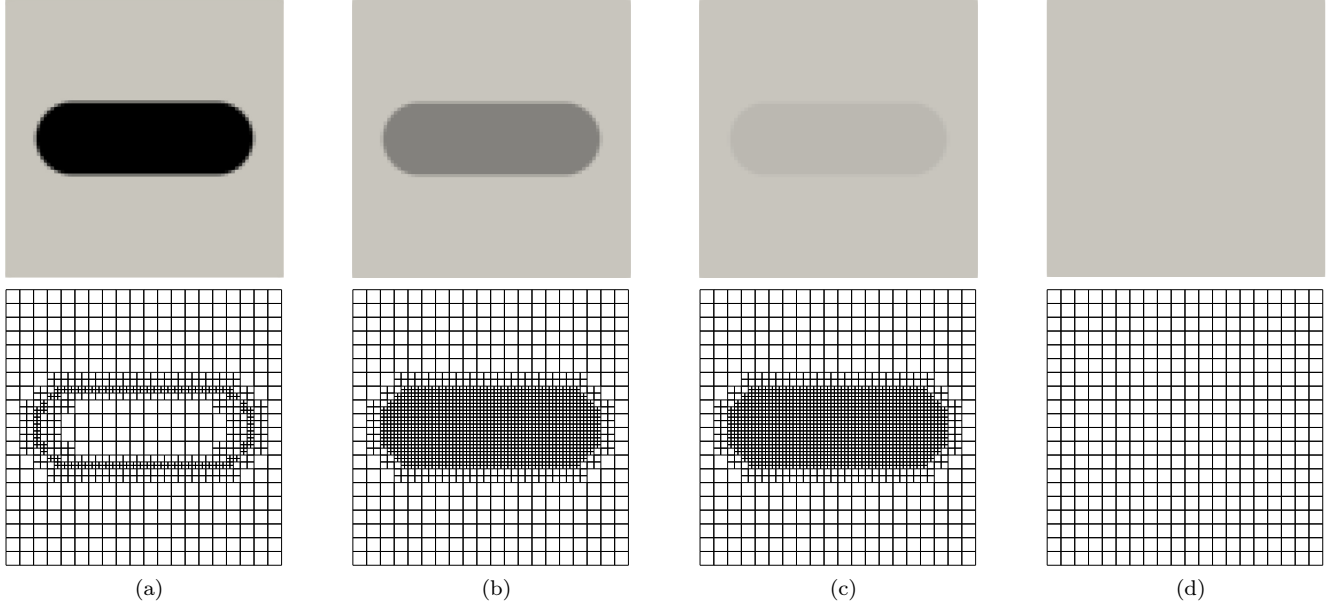


Figure 5: Effect of the size variable on a two-level adaptive mesh refinement. Effective density (top) and refined mesh (bottom) for bars with size variables α of a) 1.0, b) 0.7, c) 0.4 and d) 0.0.

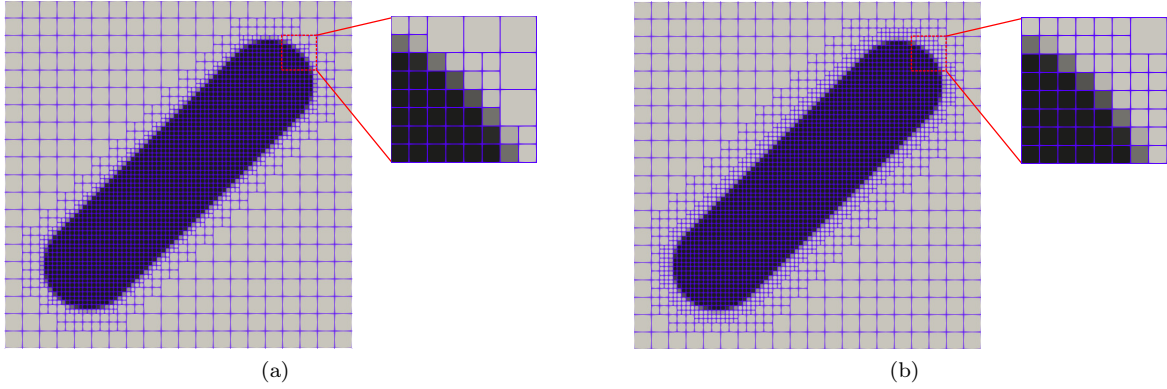


Figure 6: Element refinement along the component boundary: (a) Inconsistent (b) Consistent.

timates the true maximum. To see why this is important, we consider the case where several bars overlap at the centroid of an element e , with one of them having a size variable of $\alpha = 1$ and the others having $\alpha < 1$. If we use the true maximum function to perform the Boolean union, then the composite density would equal unity and therefore the element would not be marked for refinement per Eq. 8, which is the behavior we desire because our main goal is to reduce the mesh size as much as possible. However, when using the lower-bound KS approximation of the maximum, then $\tilde{\rho}_{ks}^e < 1$, hence it is possible that $\tilde{\rho}_{ks}^e < \rho_{th}$ in spite of the presence of the fully solid bar, and the element gets marked for refinement. Therefore, we should not choose a threshold ρ_{th} too close to unity to avoid this situation. The value $\rho_{th} = 0.9$ is used in all the examples presented in this work and performed relatively well. Fig. 8 illustrates the use of the composite density as a refinement criterion for multiple bars, with several values of the size variable of one of the bars. As seen in the figure, when both bars have a size variable of unity, the entire region inside of their union has a coarse mesh; when one of the bars has an intermediate value, the portion of that bar that does not intersect the other bar results in a fine mesh; and when the size variable of that bar is zero, it has no effect on the mesh refinement, because in that case the composite density equals the effective density of the other bar.

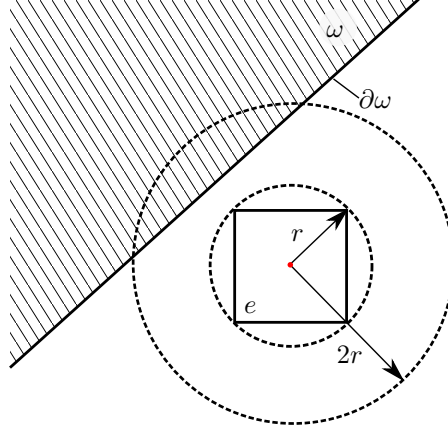


Figure 7: Consistent mesh size along boundary obtained by enlarging sampling window.

4 Optimization problems and computer implementation

To demonstrate the effectiveness of the proposed AMR method with discrete geometric components, we consider two optimization problems: 1) a minimum compliance problem; and 2) a stress-constrained problem. For the compliance-based problem, we consider the minimization of the structural compliance subject to a volume constraint, formulated as:

$$\min_{\mathbf{z}} C(\mathbf{u}) := \int_{S^t} \mathbf{u} \cdot \mathbf{t} \, da \quad (9)$$

subject to:

$$v_f(\mathbf{z}) \leq v_f^* \quad (10)$$

$$\mathbf{a}(\mathbf{u}, \mathbf{v}) = \mathbf{l}(\mathbf{v}) \quad \mathbf{u}, \forall \mathbf{v} \in \mathcal{U}_{ad} \quad (11)$$

$$\underline{\mathbf{z}} \leq \mathbf{z} \leq \bar{\mathbf{z}} \quad (12)$$

where C denotes the structural compliance and the volume fraction v_f of the structure is computed via

$$v_f(\mathbf{z}) := \frac{|\hat{\omega}|}{|\Omega|} = \frac{1}{|\Omega|} \int_{\Omega} \tilde{\rho}_{ks}(\mathbf{x}, \mathbf{z}, 0, R) \, dv \quad (13)$$

In this equation, $\hat{\omega} = \bigcup_i \omega_i \subset \Omega$ denotes the entire structure and Ω denotes the design envelope. The constraint limit on the volume fraction is denoted by v_f^* . In Eq. 11, \mathbf{a} is the energy bilinear-form and \mathbf{l} is the load linear-form given by

$$\mathbf{a}(\mathbf{u}, \mathbf{v}) := \int_{\Omega} \nabla \mathbf{v} \cdot \mathbb{C}(\mathbf{x}, \mathbf{z}, s, R) \nabla \mathbf{u} \, dv \quad (14)$$

$$\mathbf{l}(\mathbf{v}) := \int_{S^t} \mathbf{v} \cdot \mathbf{t} \, da \quad (15)$$

where $\mathbf{u}, \mathbf{v} \in \mathcal{U}_{ad}$ are the displacement and test functions respectively, and $\mathcal{U}_{ad} := \{\mathbf{u} \in H^1(\Omega) : \mathbf{u} = \mathbf{0} \text{ on } S^u\}$ is the set of admissible displacements. The boundary of the structure $\partial\hat{\omega}$ is composed of the zero traction boundary S^0 , the displacement boundary S^u and the nonzero traction boundary S^t . We assume the boundaries S^0 , S^u and S^t are not empty, and that $S^u, S^t \subset \partial\Omega$ are design-independent. The lower and upper bounds on the design variables \mathbf{z} are denoted by $\underline{\mathbf{z}}$ and $\bar{\mathbf{z}}$ respectively. To improve the convergence of the optimization, all design variables are scaled to the interval $[0, 1]$. Therefore, Eq. 12 is modified as:

$$\underline{\mathbf{b}} \leq \hat{\mathbf{z}} \leq \bar{\mathbf{b}} \quad (16)$$

where $\underline{\mathbf{b}}$, and $\bar{\mathbf{b}}$ are the scaled bounds on the scaled design variables $\hat{\mathbf{z}}$. The scaling strategies for the optimization of bar, plate, curved-plate and supershape components are detailed in [3], [4], [8] and [10] respectively. In Eqs. 13 and

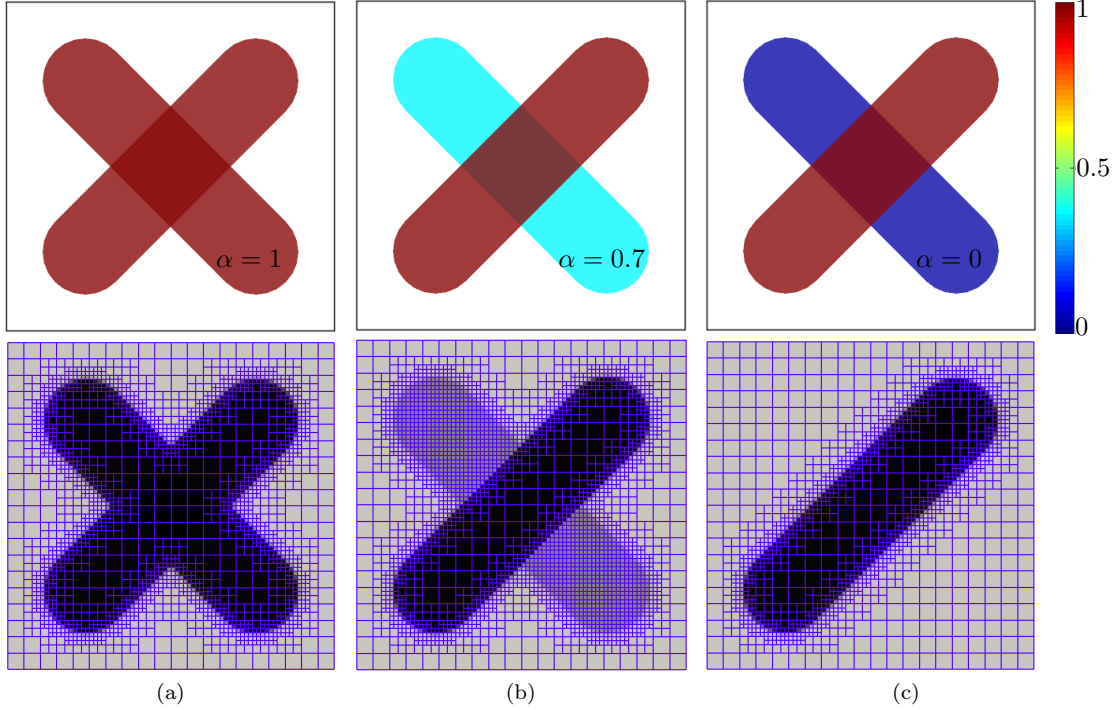


Figure 8: Mesh refinement for two intersecting bars and the effect of the size variable. Top: bars with solid colors indicating their penalized size variable values. Bottom: refined mesh with two levels of refinement and composite density. The size variable of the bar that runs from top-left to right-bottom is (a) $\alpha = 1$, (b) $\alpha = 0.7$ and (c) $\alpha = 0$.

14, R is set to $\sqrt{2}h^e/2$ for the 2-dimensional examples and $\sqrt{3}h^e/2$ for the 3-dimensional examples, corresponding to the radii of the circle and the sphere that circumscribe the square and cube elements respectively.

For the stress-based optimization problem, we consider volume minimization subject to a constraint on the maximum stress of the structure:

$$\min_{\mathbf{z}} v_f(\mathbf{z}) \quad (17)$$

subject to:

$$\max_{\mathbf{x} \in \hat{\omega}} \sigma(\mathbf{x}, \mathbf{z}) \leq \sigma^* \quad (18)$$

$$\mathbf{a}(\mathbf{u}, \mathbf{v}) = \mathbf{l}(\mathbf{v}) \quad \mathbf{u}, \forall \mathbf{v} \in \mathcal{U}_{ad} \quad (19)$$

$$\underline{\mathbf{b}} \leq \hat{\mathbf{z}} \leq \bar{\mathbf{b}} \quad (20)$$

where $\sigma(\mathbf{x}, \mathbf{z})$ is the von Mises stress at \mathbf{x} and σ^* is the maximum allowable stress. For the sake of brevity, we refer readers to [7] for details on the stress constraint of Eq. 18 and on the optimization strategies employed to solve the stress-based topology optimization problem with geometric components.

We use the Method of Moving Asymptotes (MMA) in [36, 37, 38] to solve the foregoing optimization problems. In specific, Caterpillar's implementation of MMA based on [37] is used, where the subproblems are solved using the L-BFGS-B method of [39] and the coefficient M is set to 10 unless otherwise stated. In addition, we impose a uniform move limit on all scaled design variables as in [3] to improve the convergence of the optimization. For a scaled design variable \hat{z} at iteration I , a move limit $0 < m \leq 1$ is imposed as

$$\max(\underline{\hat{z}}, \hat{z}^{I-1} - m) \leq \hat{z}^I \leq \min(\bar{\hat{z}}, \hat{z}^{I-1} + m) \quad (21)$$

Our code is implemented using the `deal.II` finite element library [40, 41]. The library provides mesh refinement utilities, including the handling of the resulting hanging nodes in the analysis, greatly facilitating the implementation of our proposed AMR scheme. Moreover, to ensure the efficiency of our method, we parallelize the AMR,

geometry projection, element assembly, solution of the linear system and sensitivity calculation using the parallel data structures and linear algebra software provided with the library.

The topology optimization with AMR is summarized in the flowchart of Fig. 9. Within each outer optimization loop, the mesh refinement always starts from the coarsest mesh level $L = 0$. As illustrated in the previous Section, the next mesh refinement level is obtained by marking elements for refinement based on the refinement criterion and the single-level mesh-incompatibility requirement; marked elements are then refined by subdivision, and the process repeated until the desired refinement level N_{rl} is attained. Since we start from a coarse mesh at every outer optimization loop, when the design changes it is entirely possible that regions that were refined in previous design iterations are no longer refined in the current one, and thus have a coarse mesh.

We note that in density-based methods it is necessary to re-define the set of design variables every time the mesh is adapted, since the design representation is tied to the mesh; moreover, the optimization functions corresponding to different mesh discretizations are mapped from previous optimization iterations to the current to avoid having to restart MMA (cf., [34]). In the topology optimization with geometric components that we consider in this work, these strategies are unnecessary because the representation of the design is independent of the mesh. We also note that the geometry projection-based indicator of Eq. 8 provides a straightforward way of performing the AMR at each iteration of the optimization, which, as demonstrated in [29] and mentioned in Section 1, leads to better designs.

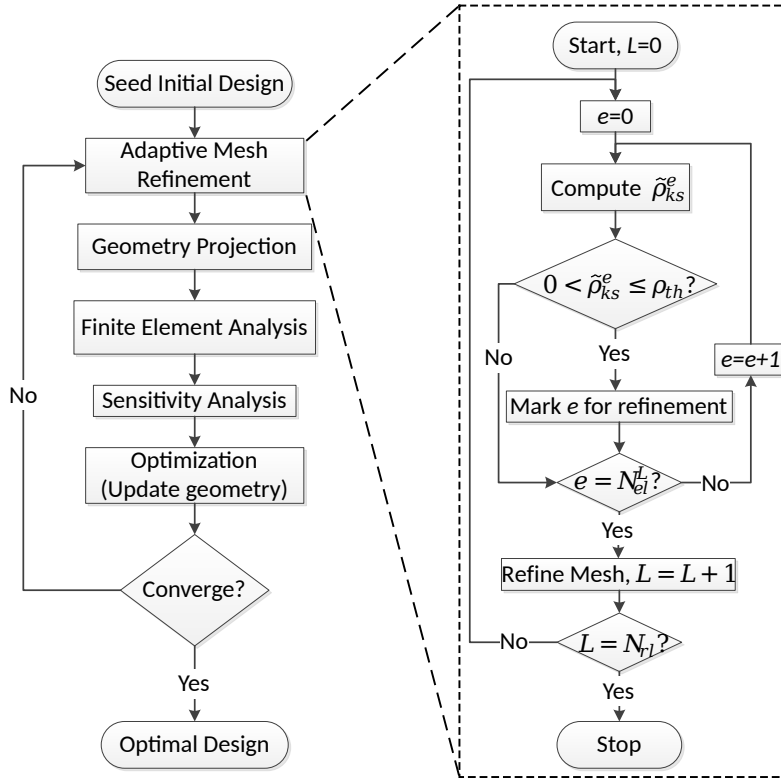


Figure 9: Flowchart of the optimization and the AMR.

The computational bottleneck of the topology optimization is the solution of the system of linear equations. For modest size problems, direct solvers can be used to efficiently solve this linear system, and they have the advantage of being less sensitive to the large condition number arising by the high-contrast between void and solid regions in topology optimization. However, for the large-scale 3-dimensional problems presented later in this paper, the use of direct solvers becomes prohibitive because of their computational and storage requirements. Iterative solvers such as the Conjugate Gradient (CG) method, on the other hand, have relatively lower computational cost and storage requirements for large problems. To achieve fast convergence for iterative solvers, a good preconditioner is necessary. Unfortunately, popular preconditioners such as incomplete Cholesky and Jacobi are very sensitive to the condition number of the system. This problem is exacerbated in the topology optimization with geometric components, because when the components do not form a connected load path between the points of application of the loads and the displacement boundary conditions, the conditioning of the system substantially worsens.

Moreover the conditioning of the system also worsens with an increased number of elements. As the condition number increases, the solution will require more iterations to converge, which makes the solution time infeasible. Therefore, it is desired to have a preconditioner for the iterative solution for large-scale problems that is less sensitive to the condition number and that scales well with the problem size. As shown in [42], the Geometric MultiGrid (GMG) preconditioner with CG provides superior performance for the solution of the linear systems arising in topology optimization. A framework of the GMG preconditioner on adaptively refined meshes is proposed in [43] and implemented in the `deal.II` library; we employ it for the 3-dimensional examples to speed up the solution process.

5 Examples

We present several numerical examples to demonstrate the proposed method. For all the examples, we consider all geometric components to be made of a homogeneous, isotropic, linear elastic material with Young’s modulus $E = 1\text{E}5$ and Poisson’s ratio $\nu = 0.3$. We employ bar and plate components for the 2-dimensional and 3-dimensional design problem respectively. The design envelope is discretized with bilinear quadrilateral elements for the 2-dimensional problems, and with trilinear hexahedral elements for the 3-dimensional problems. As aforementioned, we employ a direct solver for the 2-dimensional problems, and an iterative solver (preconditioned conjugate gradient) for the 3-dimensional problems. We impose the lower bound $\rho_{\min} = 1\text{E-}4$ on the void region (cf. Eq. 6). The optimization is stopped when the absolute value of the maximum change in the scaled design variables between the current iteration and two previous consecutive iterations is less than $5\text{E-}3$. All the 2-dimensional examples are performed using a single thread on an 8-core 3.60GHz Intel Core i7-7820X processor. The machine information for the 3-dimensional problems will be described separately for each example.

5.1 2-dimensional MBB beam design for compliance minimization

We consider the well-known Messerschmitt-Bölkow-Blohm (MBB) beam design problem shown in Fig. 10 for the first example. The optimization problem is the minimization of the structural compliance subject to a volume fraction constraint $v^* = 0.3$ (Eq. 13). Since the loading and boundary conditions are symmetric with respect to the center plane of the beam (indicated by a dashed line in Fig. 10), we only model the right-hand side of the beam. The design envelope, initial design, external loading and boundary conditions for the half-beam are shown in Fig. 11. The applied load F has a magnitude of 10. The move limit m in Eq. 21 is set to 0.05. In this example, the coarsest mesh level, corresponding to $L = 0$, is a uniform mesh with element size $h_c = 0.25$. The target refinement level N_{rl} is set to 2 so that the finest mesh element has size $h = 0.0625$ after the AMR. The strategy described in Section 3 and Fig. 9 is used to generate the adaptively refined mesh at each optimization iteration.

The AMR mesh and composite density for the initial design, iterations 10 and 30, and the last iteration (50) are plotted in Fig. 12a. The design iterates show that the mesh is adaptively refined as the optimization progresses. The region with intermediate density is meshed with a fine mesh, while regions with zero or near-unity density are meshed using coarse elements. The optimization converges to a design with compliance $C = 0.534$ in 166 seconds and the mesh in the last iteration consists of 10,756 elements. We perform the optimization for the same problem on a uniform fine mesh with element size $h = 0.0625$ and a total 25,600 elements. This full-resolution mesh is obtained by globally refining the coarsest mesh N_{rl} times before the optimization (we use this same procedure for the full-resolution meshes in this and all of the following examples). The mesh and composite density for the initial design, iterations 10 and 30, and the last iteration (42) are plotted in Fig. 12b. The entire optimization takes 171 seconds to converge to a design with $C = 0.539$, which is fairly similar to the one obtained with AMR. Moreover, the two designs are fairly similar. The average solution time per iteration is 3.3 seconds for AMR and 4.1 seconds with the full-resolution mesh. The timing information for the last optimization iteration is shown in Tab. 1.

In this example, using AMR does not significantly reduce the total optimization time, because the mesh refinement itself takes about 40% of the total time for this small problem. Nevertheless, AMR successfully halves the number of mesh elements, which reduces the computational burden for any calculation that is a function of the number of mesh elements, including the geometry projection and its sensitivities, the global stiffness matrix computation and the finite element analysis. As a result, using AMR still outperforms using the full-resolution mesh despite the overhead time associated with the AMR. As we demonstrate in other examples, however, the savings achieved by using AMR is significant for large-scale problems.

Since the bars in the design are directly represented by the design parameters, we can easily translate the optimal design into a CAD model. The composite density field and its corresponding CAD model for the optimal designs obtained using AMR and full-resolution meshes are shown in Figs. 13a and 13b respectively.

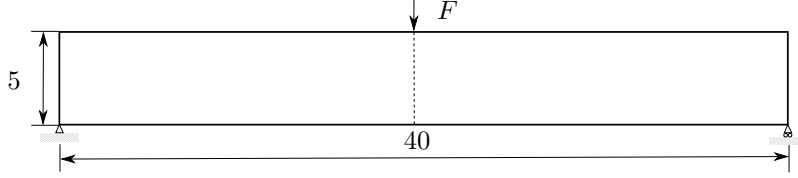


Figure 10: MBB beam design problem definition

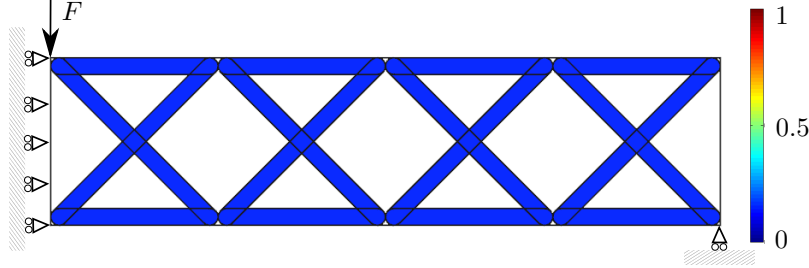


Figure 11: Initial design, geometry, loads and boundary conditions for the half-MBB beam design problem. Color denotes the penalized size variable α^s .

5.2 Stress-constrained 2-dimensional L-bracket design

In this example, we demonstrate the proposed AMR method in the context of stress-based optimization. We consider the classical L-bracket design problem that minimizes volume fraction with a constraint on the highest von Mises stress in the structure. The optimization problem is described in Eqs. 17 to 20. The design envelope, loading, boundary conditions and initial design are shown in Fig. 14. The load F has a magnitude of 3 and is distributed on several elements along the vertical edge to avoid the artificial stress concentration arising from a single concentrated load. A maximum allowable stress constraint $\sigma^* = 2.4$ is imposed. We also impose a tight move limit $m = 0.015$, to dampen detrimental design changes arising from the nonlinearity of the problem (cf., [7]). Similarly to the previous example, we perform the optimization on an adaptively refined mesh and a full-resolution mesh for comparison. For AMR, the coarsest mesh level $L = 0$ is a uniform mesh with element size $h_c = 2$. The target refinement level N_{rl} is set to 1 so that the finest mesh element has size of $h = 1$ after AMR. In order to have a consistent loading for both optimizations, elements along the loading edge have an element size $h = 1$ throughout the optimization when using AMR. The full-resolution fine mesh has a uniform mesh size $h = 1$ with a total of 6400 elements.

The optimization run with AMR takes 97 iterations to converge to a design with $v_f = 0.229$ as shown in Fig. 15a. It takes 120 seconds to converge, and the final adaptively refined mesh has 4006 elements, which roughly corresponds to two thirds the number of elements of the full-resolution mesh. Fig. 15b shows for comparison the optimal design obtained with the full-resolution mesh, which takes 117 iterations to converge to a design with $v_f = 0.227$ in 159 seconds. We observe that both approaches obtain similar designs with similar stress distributions. This example demonstrates that the proposed AMR strategy can be applied to stress-based optimization. We note that the recently published method in [34] investigates an AMR strategy to improve the accuracy of the stress computation in density-based topology optimization. However, such a consideration is out of the scope of this paper, and our goal is simply to reduce the number of elements for large-scale problems.

5.3 Stress-constrained 3-dimensional L-bracket design

We now show another example of stress-based topology optimization using AMR, this time on a 3-dimensional problem. We generate the design envelope for this problem by extruding the 2-dimensional L-bracket of the previous example by 40 units. The loading and boundary conditions are shown in Fig. 16a. A distributed surface load is applied over the shaded area near the tip of the beam, as depicted in Fig. 16a, to avoid artificial stress concentrations. The optimization consists of minimizing the volume fraction v_f with a maximum allowable stress constraint $\sigma^* = 0.15$. The coarsest mesh level $L = 0$ corresponds to a uniform mesh with element size $h_c = 4$, while the target refinement level N_{rl} is set to 2 so that the finest mesh element has size of $h = 1$ after AMR. As in the previous example, elements on the loading surface are fixed and have an element size of $h = 1$ throughout the optimization when using AMR in order to have a consistent loading. We employ the geometric multigrid preconditioner described in Sec. 4 for the solution of the analysis. As in the previous examples, we perform two optimizations using AMR

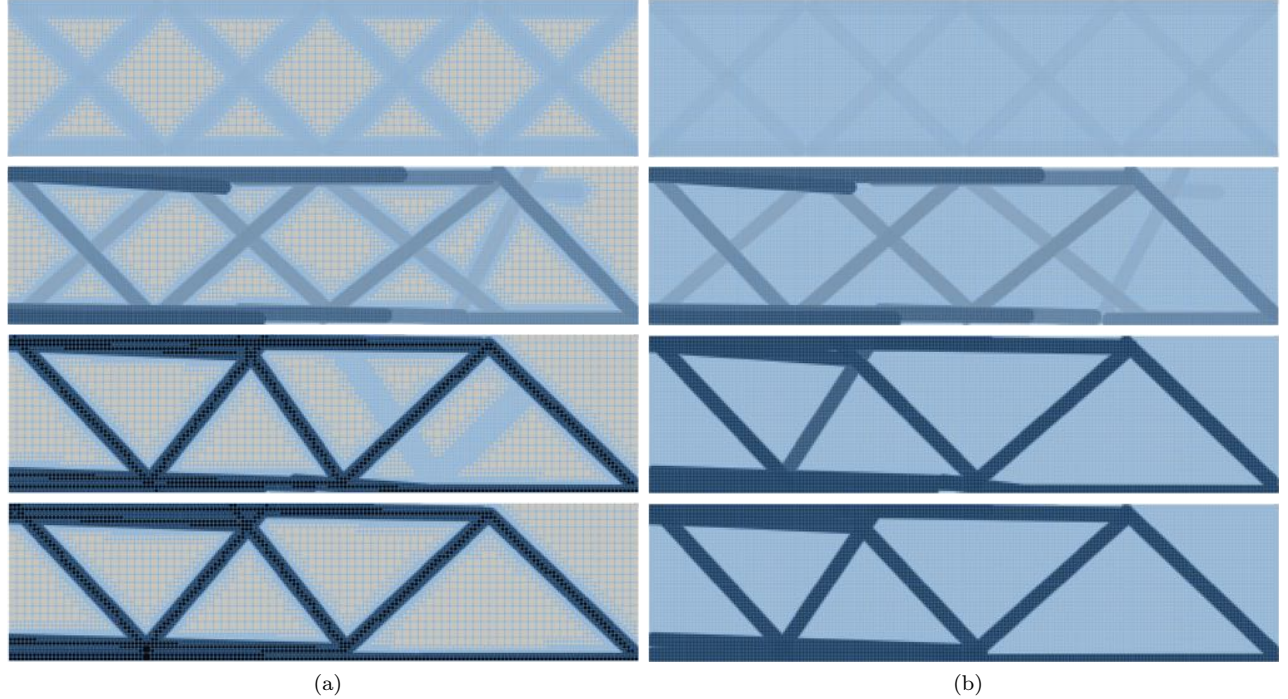


Figure 12: MBB beam design optimization with AMR (left) and full-resolution (right) meshes. From top to bottom: initial design, iteration 10, iteration 30, and last iteration (50 for AMR and 42 for full-resolution mesh). Compliance values for optimal designs are $C = 0.534$ for AMR and $C = 0.539$ for full-resolution mesh.

Task	AMR (s)	Full resolution (s)	AMR % Improvement
Mesh refinement	0.913	0	-
Geometry projection	0.254	0.514	51%
Finite element assembly	0.055	0.116	53%
Finite element linear solution	0.114	0.784	85%
Responses calculation	0.001	0.001	0%
Sensitivities calculation	1.040	1.560	33%
Total time	2.337	2.975	21%

Table 1: Time breakdown for the last iteration of the MBB problem.

and full-resolution meshes for comparison. The full-resolution mesh is a uniform mesh with element size of $h = 1$ and a total of 256,000 elements. For this example, we use four machines with 24 Xeon E5-2690 v3 2.60GHz cores each, and we employ one thread per core, for a total of 96 threads.

Fig. 17 shows the finite element mesh, the composite density iso-surface of $\tilde{\rho} = 0.4$, the CAD model and the stress distribution of the optimal designs for the two optimizations. The optimization with AMR takes 237 iterations to converge to a design with $v_f = 0.215$ in 18,000 seconds (5 hours). The adaptive mesh for the optimal design using AMR has 157,321 elements. The optimization with the full-resolution mesh converges to a design with $v_f = 0.212$ in 213 iterations and 3,840 seconds (1.07 hours). It may seem surprising at first that the optimization with the full-resolution mesh is much faster than the one using AMR despite having far more elements. The reason for this is that the local mesh refinement in AMR leads to a less efficient GMG preconditioner than the one obtained for the full-resolution mesh, which is obtained by globally refining the coarsest mesh N_{rl} times. This is evident from the comparison of the timing information shown in Tab. 2. The AMR leads to time savings for most of the tasks except the finite element linear solution and the sensitivity analysis, which, when using iterative solvers, requires another full-fledged finite element solution. Therefore, we note that for 3-dimensional problems that have a modest size, like the one presented here, the savings from using AMR cannot compensate the loss in the effectiveness of the GMG preconditioner when compared to the full-resolution uniform mesh. However, as the problem size increases, the AMR with GMG will eventually outperform the full-resolution mesh with GMG simply because of the substantial

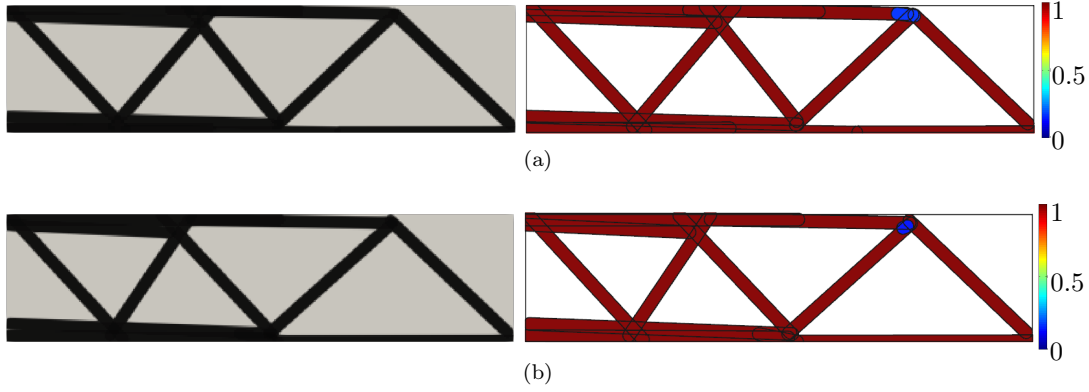


Figure 13: (a) Optimal design obtained using (a) AMR; (b) full-resolution mesh. Color denotes the penalized size variable α^s .

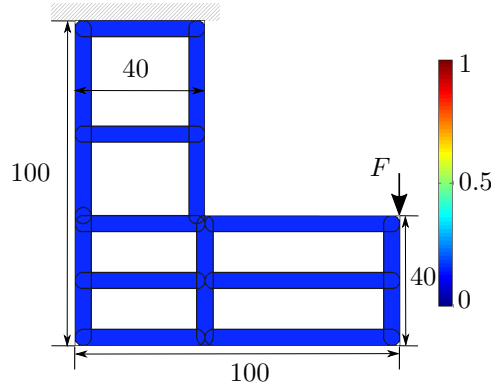


Figure 14: Initial design, geometry, loads and boundary conditions for the 2-dimensional L-bracket design problem. Color denotes the penalized size variable α^s .

reduction in the number of elements.

Task	AMR (s)	Full resolution (s)	AMR % Improvement
Mesh refinement	1.78	0	-
Geometry projection	0.238	0.259	8%
Finite element assembly	0.275	0.398	31%
GMG preparation	0.891	1.045	15%
Finite element linear solution	55.6	10.2	-445%
Responses calculation	0.184	0.267	31%
Sensitivities calculation	32.9	10.9	-202%
Total time	91.868	23.069	-298%

Table 2: Time breakdown for the last iteration of the 3-dimensional L-bracket problem.

5.4 Compliance minimization of 3-dimensional cantilever beam

In this last example, we consider the design of a 3-dimensional cantilever beam to minimize its structural compliance subject to a relatively low volume fraction constraint of $v^* = 0.05$. The design envelope, loading, boundary conditions and initial design are shown in Fig. 18a. The initial design is made of eight plates. The applied load F has a magnitude of 10. The MMA coefficient M is set to 100 to better satisfy the volume fraction constraint, and we use a move limit $m = 0.05$. We impose lower bounds $l_{\min} = 2$ and $w_{\min} = 2$ on the dimensions of plates. The placement constraint introduced in [4] is imposed for this example to ensure plates are entirely contained within the design envelope and avoid impractical cuts across the plate thickness (we refer the reader to the aforementioned publication for details). All plates have a very small fixed thickness $t = 0.2$ compared to the

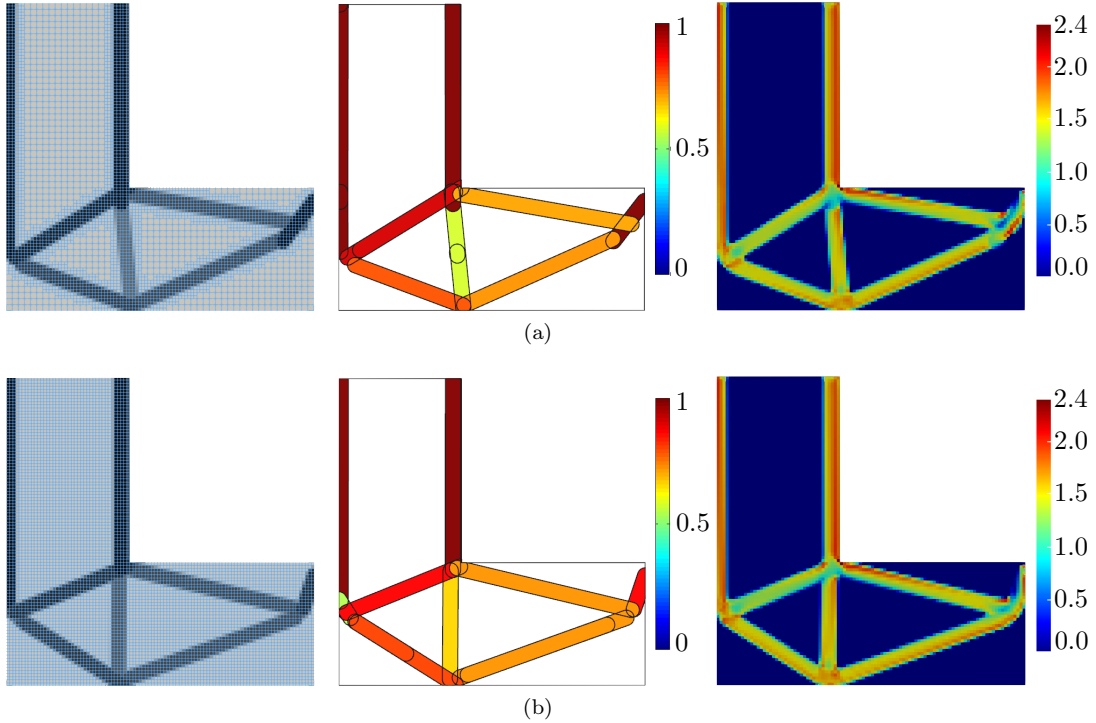


Figure 15: (a) Optimal design and its relaxed stress distribution obtained using (a) AMR, with $v_f = 0.229$; and (b) a full-resolution mesh, with $v_f = 0.227$.

dimensions of the design envelope. This high contrast between the plates thickness and the dimensions of the design envelope is common in the design of structures made of stock plates. For this example, the coarsest mesh ($L = 0$) has a uniform element size $h_c = 1$ as shown in Fig. 18b. We target an element size $h = 0.03125$ that requires $N_{rl} = 5$ levels of refinement. If the mesh were globally refined five times to obtain the full-resolution mesh as in previous examples, the refinement would result in 23,592,960 uniform mesh elements. However, by employing the proposed AMR strategy, the number of elements reduces to 3,294,920 for the same problem (for the initial design).

For this example, we use six machines with 24 Xeon E5-2690 v3 2.60GHz cores each, and we employ one thread per core, for a total of 144 threads. We apply the AMR strategy to this example; Fig. 19 shows the final design. The optimization takes 231 iteration in 665 minutes (11 h 5 min) to converge, hence an optimization iteration spends 2.9 minutes on average. The adaptively refined mesh for the last iteration is shown in Fig. 20. The total number of elements for this last iteration is 1,976,155, which corresponds to only 8.4% of the full-resolution mesh. Fig. 21 depicts the history of the number of mesh elements during the entire optimization. For comparison, we also perform one design iteration with the full-resolution mesh: we take the optimal design of Fig. 19 obtained using AMR, refine all elements to the highest refinement level to obtain the full-resolution mesh, and perform one design step. If the optimization with the full-resolution mesh were to take the same number of iterations as that with the AMR strategy, the total optimization time would be approximately 42.5 hours (the actual time will be different since the condition number of the system is different for each design and therefore the number of iterations to convergence of CG will vary). The timing information is summarized and compared in Tab. 3. From this table, we can observe that AMR leads to speedups in every task, resulting in an estimated 74% time savings per optimization iteration. However, it is worth noting that the savings obtained from AMR in the linear solution task is not significant. The GMG preconditioner obtained from the full-resolution mesh is so efficient that it can solve a 23 M elements mesh in approximately seven minutes. However, the solution time with the AMR mesh is still much shorter than with the full-resolution mesh. We note that in the case of unstructured meshes, the efficiency of the GMG preconditioner is limited, hence we expect a better speedup using AMR [44].

Unfortunately, there is no rule to determine a priori if performing AMR is more efficient than using the full-resolution mesh, because this depends on the problem; for instance, for a design region that is not a cuboid, and/or for unstructured meshes as aforementioned, computing the GMG preconditioner on the full-resolution mesh may become more expensive, and so the AMR strategy may be advantageous for smaller problems. The only certain way to determine the convenience of using AMR is to perform a single finite element solution with both schemes

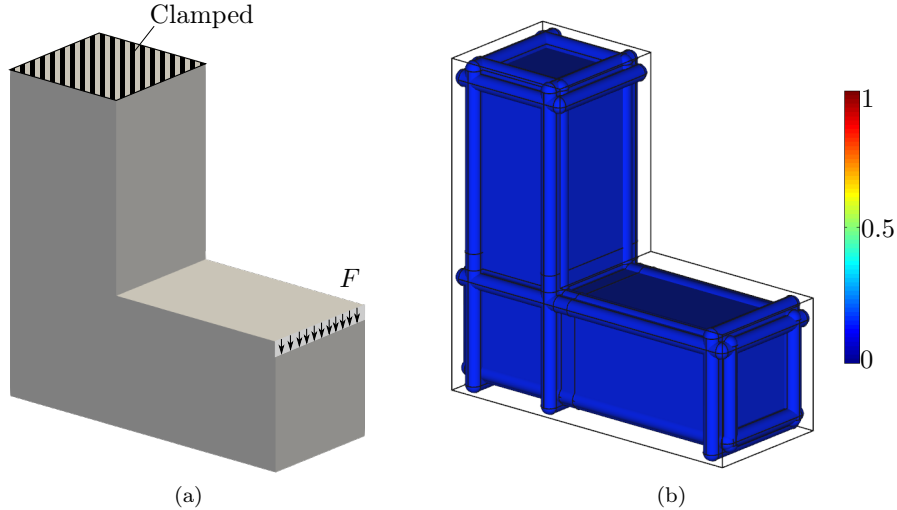


Figure 16: 3-dimensional L-bracket problem definition: (a) design space, loading and boundary conditions; (b) initial design made of 16 plates. Color scale indicates the penalized size variable α^s .

and compare the times.

Task	AMR (s)	Full resolution (s)	AMR % Improvement
Mesh refinement	11	0	-
Geometry projection	2.35	16.7	86%
Finite element assembly	2.37	22.6	90%
GMG preparation	6.16	69.22	91%
Finite element linear solution	129	436	70%
Responses calculation	0.003	0.019	84%
Sensitivities calculation	4.58	51.7	91%
Total time	155.46	596.24	74%

Table 3: Time breakdown for the last iteration of the 3-dimensional cantilever beam problem.

6 Conclusions

The presented numerical experiments show that the proposed adaptive mesh refinement strategy accommodates very well the topology optimization with discrete geometric components using the geometry projection method. The proposed strategy is independent of the shape of the geometric components, and we applied it successfully to compliance minimization and stress-constrained problems. Since the refinement indicator is based on the geometry projection, our method can readily refine the mesh at every optimization iteration, which leads to efficient designs. As shown by our examples, it does not always make sense to use this AMR strategy: for relatively small problems, or for large problems where a highly structured mesh leads to a highly efficient GMG preconditioner, the optimization with the full-resolution mesh may still outperform the optimization with the adaptively refined mesh. However, for some of the problems we are interested in, namely problems with very slender members in relation to the dimensions of the design envelop and with relatively low volume fractions, the required full-resolution meshes are so large that the AMR strategy is bound to outperform the optimization with the full-resolution mesh. In these cases, the AMR clearly achieves our goal of substantially decreasing the computational burden. Additional future work is required to incorporate in our refinement strategy a refinement indicator based on solution error.

Acknowledgements

Support from Caterpillar to conduct this work is gratefully acknowledged by all authors. The last author would also like to acknowledge support from the Office of Naval Research, USA, Grant N00014-17-1-2505.

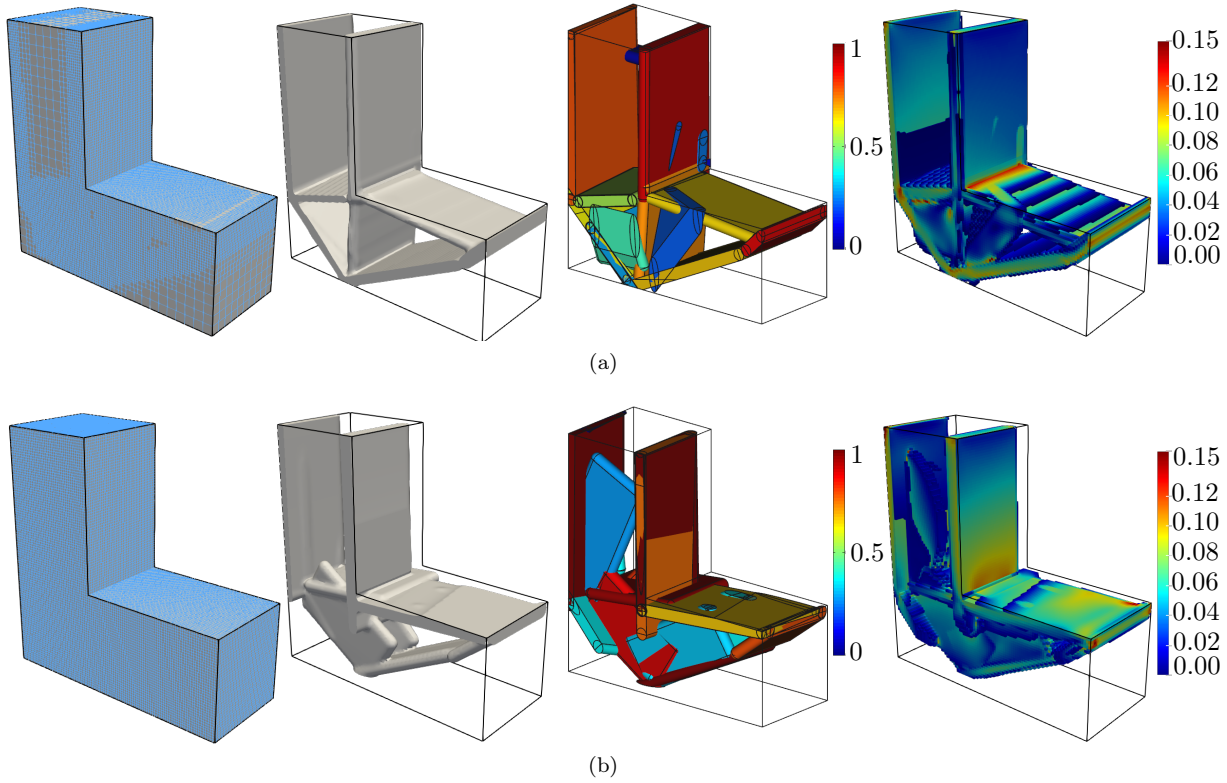


Figure 17: Results obtained for optimizations with (a) AMR, with $v_f = 0.215$; and (b) full-resolution mesh, with $v_f = 0.212$. From left to right: mesh for last iteration, composite density iso-surface of $\bar{\rho} = 0.4$, CAD representation with color indicating penalized size variable α^s , and von Mises stress.

References

- [1] Ole Sigmund and Kurt Maute. Topology optimization approaches. *Structural and Multidisciplinary Optimization*, 48(6):1031–1055, 2013.
- [2] Bryan Bell, Julian Norato, and Daniel Tortorelli. A geometry projection method for continuum-based topology optimization of structures. In *12th AIAA Aviation Technology, Integration, and Operations (ATIO) Conference and 14th AIAA/ISSMO Multidisciplinary Analysis and Optimization Conference*, page 5485, 2012.
- [3] JA Norato, BK Bell, and DA Tortorelli. A geometry projection method for continuum-based topology optimization with discrete elements. *Computer Methods in Applied Mechanics and Engineering*, 293:306–327, 2015.
- [4] Shanglong Zhang, Julián A Norato, Arun L Gain, and Naesung Lyu. A geometry projection method for the topology optimization of plate structures. *Structural and Multidisciplinary Optimization*, pages 1–18, 2016.
- [5] Jiadong Deng and Wei Chen. Design for structural flexibility using connected morphable components based topology optimization. *Science China Technological Sciences*, 59(6):839–851, 2016.
- [6] Shanglong Zhang and Julián A Norato. Optimal design of panel reinforcements with ribs made of plates. *Journal of Mechanical Design*, 139(8):081403, 2017.
- [7] Shanglong Zhang, Arun L Gain, and Julián A Norato. Stress-based topology optimization with discrete geometric components. *Computer Methods in Applied Mechanics and Engineering*, 325:1–21, 2017.
- [8] Shanglong Zhang, Arun L Gain, and Julián A Norato. A geometry projection method for the topology optimization of curved plate structures with placement bounds. *International Journal for Numerical Methods in Engineering*, 114(2):128–146, 2018.

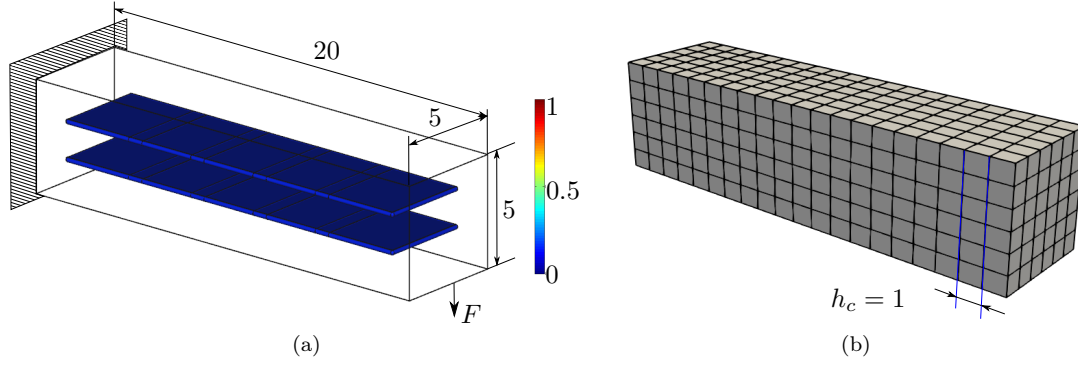


Figure 18: (a) Initial design, geometry, loads and boundary conditions for the 3-dimensional cantilever beam design problem. Color denotes the penalized size variable α^s . (b) Initial coarse mesh.

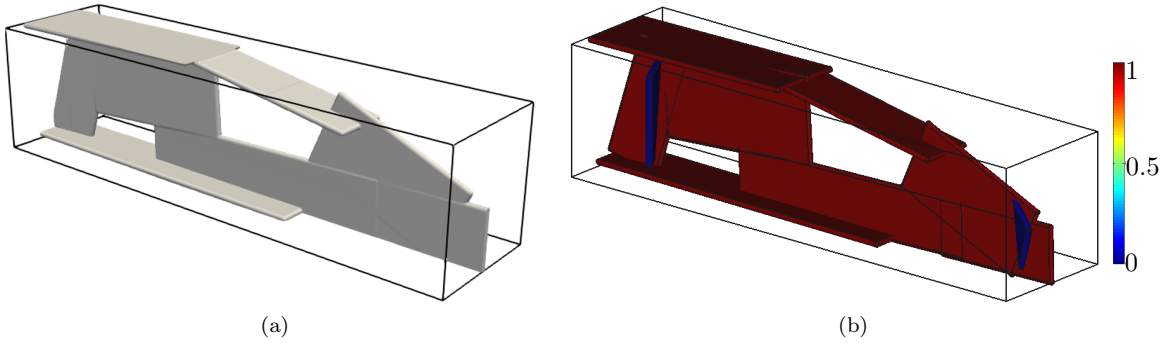


Figure 19: Final design of 3-dimensional cantilever beam: (a) 0.4 iso-surface of composite density, $C = 2.71$; and (b) plate design, with colors indicating the penalized size variable α^s .

- [9] Hesaneh Kazemi, Ashkan Vaziri, and Julián A Norato. Topology optimization of structures made of discrete geometric components with different materials. *Journal of Mechanical Design*, 140(11):111401, 2018.
- [10] Julián A Norato. Topology optimization with supershapes. *Structural and Multidisciplinary Optimization*, 58(2):415–434, 2018.
- [11] Seth Watts and Daniel A Tortorelli. A geometric projection method for designing three-dimensional open lattices with inverse homogenization. *International Journal for Numerical Methods in Engineering*, 112(11):1564–1588, 2017.
- [12] Xu Guo, Weisheng Zhang, and Wenliang Zhong. Doing topology optimization explicitly and geometrically—a new moving morphable components based framework. *Journal of Applied Mechanics*, 81(8):081009, 2014.
- [13] Xu Guo, Weisheng Zhang, Jian Zhang, and Jie Yuan. Explicit structural topology optimization based on moving morphable components (MMC) with curved skeletons. *Computer methods in applied mechanics and engineering*, 310:711–748, 2016.
- [14] Weisheng Zhang, Dong Li, Jian Zhang, and Xu Guo. Minimum length scale control in structural topology optimization based on the moving morphable components (MMC) approach. *Computer Methods in Applied Mechanics and Engineering*, 311:327–355, 2016.
- [15] Xu Guo, Jianhua Zhou, Weisheng Zhang, Zongliang Du, Chang Liu, and Ying Liu. Self-supporting structure design in additive manufacturing through explicit topology optimization. *Computer Methods in Applied Mechanics and Engineering*, 323:27–63, 2017.
- [16] Weisheng Zhang, Wanying Yang, Jianhua Zhou, Dong Li, and Xu Guo. Structural topology optimization through explicit boundary evolution. *Journal of Applied Mechanics*, 84(1):011011, 2017.

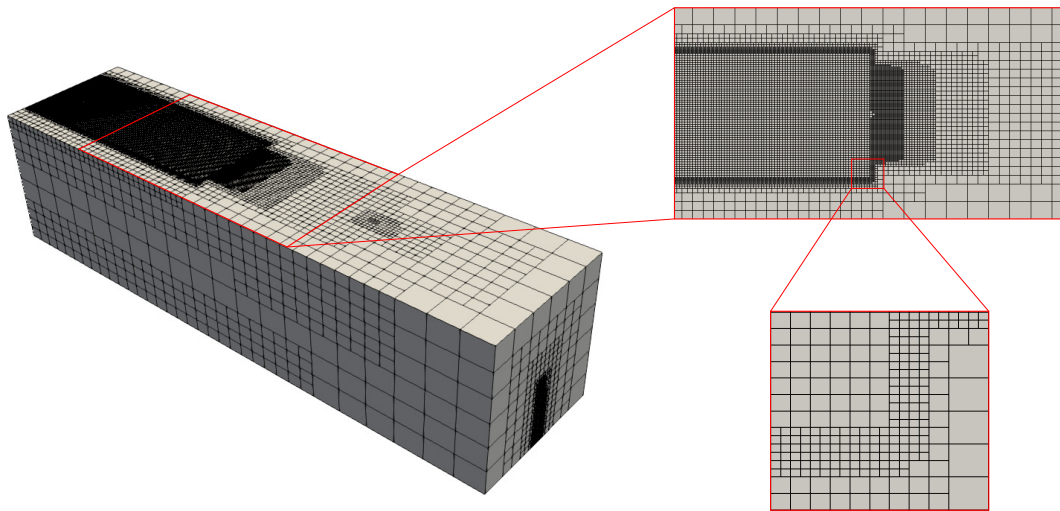


Figure 20: Adaptively refined mesh of the design in the last iteration of the 3-dimensional cantilever beam optimization using AMR.

- [17] Van-Nam Hoang and Gang-Won Jang. Topology optimization using moving morphable bars for versatile thickness control. *Computer Methods in Applied Mechanics and Engineering*, 317:153–173, 2017.
- [18] Weisheng Zhang, Junfu Song, Jianhua Zhou, Zongliang Du, Yichao Zhu, Zhi Sun, and Xu Guo. Topology optimization with multiple materials via moving morphable component (MMC) method. *International Journal for Numerical Methods in Engineering*, 113(11):1653–1675, 2018.
- [19] Weisheng Zhang, Ying Liu, Zongliang Du, Yichao Zhu, and Xu Guo. A moving morphable component based topology optimization approach for rib-stiffened structures considering buckling constraints. *Journal of Mechanical Design*, 140(11):111404, 2018.
- [20] Weisheng Zhang, Jishun Chen, Xuefeng Zhu, Jianhua Zhou, Dingchuan Xue, Xin Lei, and Xu Guo. Explicit three dimensional topology optimization via moving morphable void (mmv) approach. *Computer Methods in Applied Mechanics and Engineering*, 322:590–614, 2017.
- [21] Weisheng Zhang, Dong Li, Jianhua Zhou, Zongliang Du, Baojun Li, and Xu Guo. A moving morphable void (MMV)-based explicit approach for topology optimization considering stress constraints. *Computer Methods in Applied Mechanics and Engineering*, 334:381–413, 2018.
- [22] K. Maute and E. Ramm. Adaptive topology optimization. *Structural Optimization*, 10(2):100–112, 1995. ISSN 09344373. doi: 10.1007/BF01743537.
- [23] Joao Carlos Arantes Costa and Marcelo Krajnc Alves. Layout optimization with h-adaptivity of structures. *International Journal for Numerical Methods in Engineering*, 58(1):83–102, 2003. ISSN 00295981. doi: 10.1002/nme.759.
- [24] Roman Stainko. An adaptive multilevel approach to the minimal compliance problem in topology optimization. *Communications in Numerical Methods in Engineering*, 22(2):109–118, 2006. ISSN 10698299. doi: 10.1002/cnm.800.
- [25] Matteo Bruggi and Marco Verani. A fully adaptive topology optimization algorithm with goal-oriented error control. *Computers and Structures*, 89(15-16):1481–1493, 2011. ISSN 00457949. doi: 10.1016/j.compstruc.2011.05.003. URL <http://dx.doi.org/10.1016/j.compstruc.2011.05.003>.
- [26] Mathias Wallin, Matti Ristinmaa, and Henrik Askfelt. Optimal topologies derived from a phase-field method. *Structural and Multidisciplinary Optimization*, 45(2):171–183, 2012. ISSN 1615147X. doi: 10.1007/s00158-011-0688-x.
- [27] Yiqiang Wang, Zhan Kang, and Qizhi He. Adaptive topology optimization with independent error control for separated displacement and density fields. *Computers and Structures*, 135:50–61, 2014. ISSN 00457949. doi: 10.1016/j.compstruc.2014.01.008. URL <http://dx.doi.org/10.1016/j.compstruc.2014.01.008>.

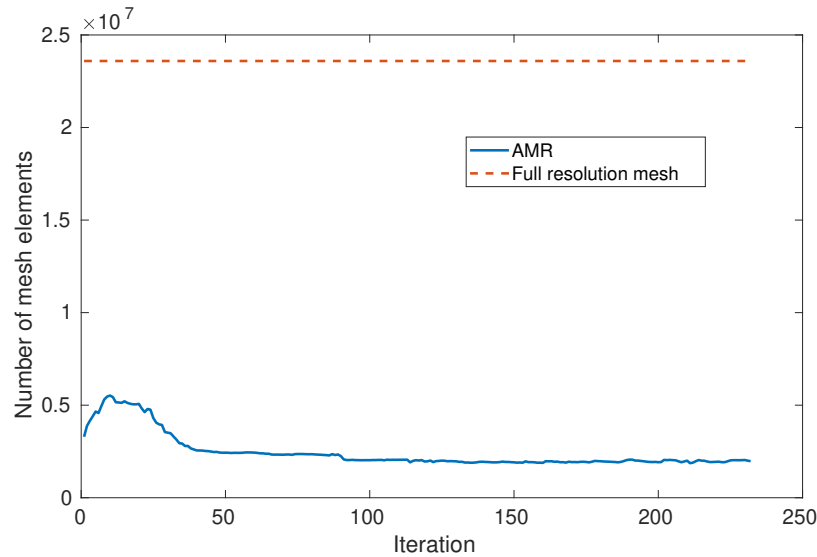


Figure 21: History of the number of elements using AMR for the 3-dimensional cantilever design problem.

- [28] H. Nguyen-Xuan. A polytree-based adaptive polygonal finite element method for topology optimization. *International Journal for Numerical Methods in Engineering*, 110(10):972–1000, 2017. ISSN 10970207. doi: 10.1002/nme.5448.
- [29] Shun Wang, Eric de Sturler, and Glaucio H Paulino. Dynamic adaptive mesh refinement for topology optimization. *arXiv preprint arXiv:1009.4975*, 2010.
- [30] Alexandre Nana, Jean Christophe Cuillière, and Vincent Francois. Towards adaptive topology optimization. *Advances in Engineering Software*, 100:290–307, 2016. ISSN 18735339. doi: 10.1016/j.advengsoft.2016.08.005. URL <http://dx.doi.org/10.1016/j.advengsoft.2016.08.005>.
- [31] Kristian Ejlebjerg Jensen. Solving stress and compliance constrained volume minimization using anisotropic mesh adaptation, the method of moving asymptotes and a global p-norm. *Structural and Multidisciplinary Optimization*, 54(4):831–841, 2016. ISSN 16151488. doi: 10.1007/s00158-016-1439-9. URL <http://dx.doi.org/10.1007/s00158-016-1439-9>.
- [32] Kristian Ejlebjerg Jensen. Anisotropic mesh adaptation and topology optimization in three dimensions. *Journal of Mechanical Design*, 138(6):061401, 2016.
- [33] Ajit Panesar, David Brackett, Ian Ashcroft, Ricky Wildman, and Richard Hague. Hierarchical remeshing strategies with mesh mapping for topology optimisation. *International Journal for Numerical Methods in Engineering*, 111(7):676–700, 2017. ISSN 10970207. doi: 10.1002/nme.5488.
- [34] Miguel A Salazar De Troya and Daniel A Tortorelli. Adaptive mesh refinement in stress-constrained topology optimization. *Structural and Multidisciplinary Optimization*, in press.
- [35] J Norato, R Haber, D Tortorelli, and Martin P Bendsøe. A geometry projection method for shape optimization. *International Journal for Numerical Methods in Engineering*, 60(14):2289–2312, 2004.
- [36] Krister Svanberg. The method of moving asymptotes—a new method for structural optimization. *International journal for numerical methods in engineering*, 24(2):359–373, 1987.
- [37] Krister Svanberg. A globally convergent version of mma without linesearch. In *Proceedings of the first world congress of structural and multidisciplinary optimization*, volume 28, pages 9–16. Goslar, Germany, 1995.
- [38] Krister Svanberg. A class of globally convergent optimization methods based on conservative convex separable approximations. *SIAM journal on optimization*, 12(2):555–573, 2002.
- [39] Richard H Byrd, Peihuang Lu, Jorge Nocedal, and Ciyu Zhu. A limited memory algorithm for bound constrained optimization. *SIAM Journal on Scientific Computing*, 16(5):1190–1208, 1995.

- [40] W. Bangerth, R. Hartmann, and G. Kanschat. deal.II – a general purpose object oriented finite element library. *ACM Trans. Math. Softw.*, 33(4):24/1–24/27, 2007.
- [41] G. Alzetta, D. Arndt, W. Bangerth, V. Boddu, B. Brands, D. Davydov, R. Gassmoeller, T. Heister, L. Heltai, K. Kormann, M. Kronbichler, M. Maier, J.-P. Pelteret, B. Turcksin, and D. Wells. The `deal.II` library, version 9.0. *Journal of Numerical Mathematics*, 2018, accepted.
- [42] Oded Amir, Niels Aage, and Boyan S Lazarov. On multigrid-CG for efficient topology optimization. *Structural and Multidisciplinary Optimization*, 49(5):815–829, 2014.
- [43] Bärbel Janssen and Guido Kanschat. Adaptive multilevel methods with local smoothing for H^1 - and H^{curl} -conforming high order finite element methods. *SIAM Journal on Scientific Computing*, 33(4):2095–2114, 2011.
- [44] Dimitri J Mavriplis. Multigrid techniques for unstructured meshes. Technical report, Institute for Computer Applications in Science and Engineering, Hampton, VA, 1995.